RSC Advances

This is an *Accepted Manuscript*, which has been through the Royal Society of Chemistry peer review process and has been accepted for publication.

Accepted Manuscripts are published online shortly after acceptance, before technical editing, formatting and proof reading. Using this free service, authors can make their results available to the community, in citable form, before we publish the edited article. This *Accepted Manuscript* will be replaced by the edited, formatted and paginated article as soon as this is available.

You can find more information about *Accepted Manuscripts* in the Information for Authors.

Please note that technical editing may introduce minor changes to the text and/or graphics, which may alter content. The journal's standard Terms & Conditions and the Ethical guidelines still apply. In no event shall the Royal Society of Chemistry be held responsible for any errors or omissions in this *Accepted Manuscript* or any consequences arising from the use of any information it contains.

ROYAL SOCIETY OF CHEMISTRY

www.rsc.org/advances

RSC Advances RSCPublishing

ARTICLE

CO_2 splitting into CO and O_2 in micro-tubular solid oxide electrolysers

Cite this: DOI: 10.1039/x0xx00000x

L. Kleiminger[a], T. Li[a], K. Li[a] and G. H. Kelsall[a]

Received 00th January 2012,
Accepted 00th January 2012

DOI: 10.1039/x0xx00000x

www.rsc.org/

Micro-tubular solid oxide electrolysers for electrochemical CO_2 reduction of the form Ni-YSZ|YSZ|YSZ-LSM|LSM have been fabricated using a two-step method: dual layer co-extrusion phase inversion to produce electrode-supported | electrolyte precursors and subsequent coating with the outer electrode, whereby each step was followed by (co-)sintering. The microstructures and physical properties of the fibres were characterized and the electrochemical performance of the fabricated electrolysers determined. Electrolyte thicknesses of 19 (± 2), 26 (± 2) and 49 (± 3) µm were achieved. Electrolysis performance increased with increasing temperature (700-800 °C) and with decreasing electrolyte thickness. The maximum performance achieved was 1.0 A cm^{-2} at 1.8 V cell potential difference at 800 °C for a 15 µm electrolyte. Electrical impedance spectroscopy revealed that only 5-28% of the ohmic polarization resistance was due to the electrolyte resistance; most of the resistance was due to electrical connections and contact potential losses. The feasibility to operate the solid oxide cells in electrolysis and fuel cell modes was demonstrated, revealing that no unique gas composition existed that would optimise the performance in both modes simultaneously.

Introduction

With the objective of moving towards minimising carbon emissions during energy conversion, the need for large-scale storage becomes essential because of the dynamics of energy demand and the intermittency of renewable energy sources, such as wind or solar. However, the installed capacity of electrical energy storage (e.g. batteries or pumped hydro) is limited compared to power demand variations; the daily power demand fluctuations in the UK are 20 GW, compared to a storage capacity of 15 GW h [1,2]. Therefore, fixing electrical energy in chemical bonds for future re-generation of electricity using electrolysis of CO_2 and/or H_2O is a promising technology to achieve a closed carbon loop and to maintain current atmospheric CO_2 levels, if powered by renewable sources. Goeppert *et al.* [3] reviewed technologies for the capture of CO_2 from the air highlighting its potential feasibility, which could provide a renewable feedstock of CO_2 in the future.

Solid oxide electrolysers (SOEs) offer thermodynamic and kinetic benefits due to elevated operating temperatures > 700ºC, as electrical energy input can be substituted in part by thermal energy [4]. Furthermore, higher temperatures accelerate charge transfer reactions and mass transport rates and decrease electrolyte resistance. The proposed reaction scheme is outlined in reactions 1-4 for reversible operation (SOE storage mode and solid oxide fuel cell (SOFC) power generation mode):

Fuel electrode (e.g. Ni): $$CO_2 + 2e^- \underset{SOFC}{\overset{SOE}{\rightleftarrows}} CO + O^{2-} \quad (1)$$

Electrolyte (e.g. YSZ): $$O^{2-}(\text{cathode}) \underset{SOFC}{\overset{SOE}{\rightleftarrows}} O^{2-}(\text{anode}) \quad (2)$$

Air electrode (e.g. LSM): $$\tfrac{1}{2}\left(2O^{2-} \underset{SOFC}{\overset{SOE}{\rightleftarrows}} O_2 + 4e^-\right) \quad (3)$$

Overall: $$CO_2 \underset{SOFC}{\overset{SOE}{\rightleftarrows}} CO + \tfrac{1}{2}O_2 \quad (4)$$

CO_2 electrolysis has been studied widely on planar cells for different cathode materials, including variations on nickel cermets (e.g. Ni-YSZ, Ni/Ru-GDC) as well as alternative cermets (e.g. Cu-CGO) or infiltrated scaffolds (e.g. Pd-LSCM-CZY) [5-9]. However, the focus of the presently reported research is the reactor design and novel fabrication method, decreasing the required number of fabrication steps. Thus, a Ni-YSZ cermet fuel electrode was chosen, as the sintering temperatures of Ni and YSZ are compatible and no solid state reactions under normal operation conditions have been reported [10].

The advantage of tubular cells is increased robustness to thermal cycling, fast start-up and more facile sealing [11, 12]. High temperature electrolysis using a tubular reactor design is not a novel concept; in the 1980s, the HOT ELLY project in Germany focused on hydrogen generation using tubular stacks

RSC Advances Accepted Manuscript

Nomenclature

Symbol	*Meaning*	*Units*
A_m	Membrane area ($A_m=[2\pi((r_e+t_e)-r_e)L_f]/\ln((r_e+t_e)/r_e)$)	m^2
A_w	Cross-section of wires	m^2
D_{eff}	Effective diffusion coefficient	$m^2\ s^{-1}$
D_{i-j}	Binary diffusion coefficient	$m^2 s^{-1}$
D_i, D_o	Inner and outer fibre diameter, respectively	M
dn/dt	change in reactant-product (e.g. CO_2-CO)	mol s^{-1}
E	Activation energy	J mol^{-1}
ΔE_{tn}	Thermo-neutral potential difference	V
ΔE	Equilibrium potential	V
F	Faraday constant (96485)	C mol^{-1}
F_f	Fracture force	N
ΔH_r	Enthalpy of reaction	J mol^{-1}
I	Total current	A
J	Current density	A cm^{-2}
j_L	Mass transport limited current density	A cm^{-2}
L_e	Electrode length	M
L_f	Length of fibre	M
L_w	Length of wires	M
M	Molecular weight	g mol^{-1}
P	Permeability	mol $m^{-2}\ s^{-1}$ Pa s^{-1}
P	Pressure (with e.g. i=initial, a=atmospheric, f=final)	Pa
p_x	Partial pressures (of CO_2, CO, O_2)	Pa
R	Universal gas constant (8.3145)	J $mol^{-1}\ K^{-1}$
R_o	Total cell ohmic polarization resistance	Ω
r	Radius of fibre layers	M
r_e	Radius of electrolyte	M
T	Temperature	K
t	Duration	S
t_i	Fibre layer thickness (a=anode, c=cathode, e=electrolyte)	M
U	Cell potential difference	V
V	Volume	m^3
$\dot{V}$	Volumetric flow rates	$cm^3\ min^{-1}$
v_e	Electron stoichiometry of reaction	-
w^e	Specific electrical energy consumption	kW h (t product)$^{-1}$
x_i	Species i mole fraction	-
ε	Apparent porosity	-
ρ	Density	g cm^{-3}
σ_i	conductivity of phase i	S m^{-1}
σ_f	Bending strength	Pa
τ	Tortuosity	-
Φ_i	Charge yield	-
Φ_{i-j}	Round-trip efficiency	-
$\Delta\phi$	Ohmic potential loss	V

based on an YSZ electrolyte [13, 14]. Simultaneously, the tubular Westinghouse-designed fuel cells were tested in electrolysis mode for water splitting in the USA [15]. However, the renaissance of high temperature electrolysis occurred only recently with the increased share of renewable energy in power generation. Presently, (micro-) tubular reactors are being researched for H_2O and co-electrolysis using variations of zirconia-based electrolyte materials, employing stabilizers such as scandium or yttrium [16-19]. To maximise volumetric output power densities, the aim is to decrease the characteristic dimension of individual cells, so increasing electrode area per unit volume [11]. Various fabrication methods have been reported for these tubular reactors including ram extrusion, slip casting, dip-coating and phase inversion [16-19], whereby each layer adds an extra production step. However, the feasibility of co-extruding dual-layer hollow fibres using phase inversion, producing two layers in a single step has been demonstrated recently [20-22]. This was followed by sintering, then deposition of a second electrode and current collectors to fabricate a complete fuel cell.

In this study, the performance of CO_2 reduction to CO plus O_2 evolution has been investigated using an yttria-stabilized zirconia (YSZ) micro-tubular solid oxide electrolyser (MT-SOE). Co-extruded NiO-YSZ|YSZ dual-layer hollow fibres were fabricated using a novel phase inversion technique and were subsequently coated with a strontium doped lanthanum manganite (LSM) oxygen electrode (LSM-YSZ|LSM). The objectives were to correlate electrolyser performance with electrode microstructure, electrolyte thickness, CO_2/CO feed gas composition, operating temperature and reversibility between electrolyser and fuel cell modes.

Experimental

Fibre fabrication

The dual-layer cathode-supported hollow fibres (NiO-YSZ|YSZ) were produced using a phase inversion technique; the cathode metal oxide-ceramic (NiO-YSZ) and electrolyte ceramic (YSZ) suspensions were co-spun through a triple layer orifice into a coagulation bath, to solidify the fibre precursors by solvent exchange (Figure 1).

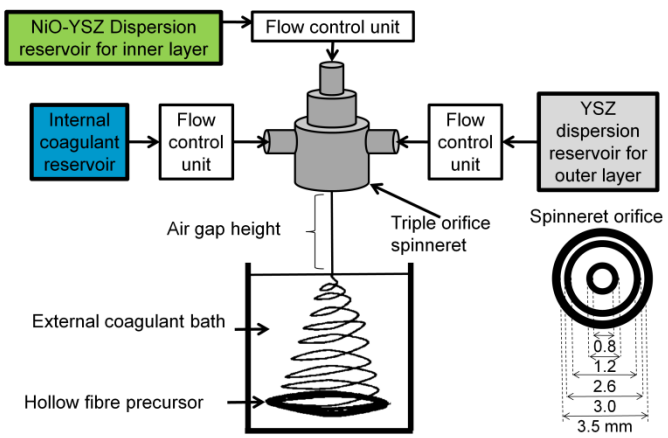

Figure 1: Phase inversion system to fabricate dual-layer hollow fibre precursors.

The inner and outer suspensions were prepared from NiO (0.5-1.5 µm particle size (d50), NexTech Materials Ltd., USA) and YSZ (8 mol% yttria doped ZrO_2, 0.9-1.2 µm particle size (d50), NexTech Materials Ltd., USA) powders dispersed in di-methyl sulfoxide (DMSO, VWR International LLC, UK) using polyethyleneglycol 30-dipolyhydroxystearate dispersant (Arlacel P135, Uniqema, Spain). After roll milling for 3-4 days polyethersulfone (PESf, Radel A-300, Ameco Performance, USA) was added as a binder and mixed further for 2-3 days to

RSC Advances Accepted Manuscript

This journal is © The Royal Society of Chemistry 2012

achieve homogeneous suspensions. Compositions of the different suspensions are summarized in Table 1.

Table 1: Compositions of the spinning suspensions for the dual-layer hollow fibres.

Material	*Inner electrode composition (wt %)*	*Electrolyte composition (wt %)*
YSZ	27.2	69.4
NiO	40.8	-
Polymer binder (PESf)	24.7	23.1
Dispersant (Arlacel P135)	6.80	6.94
Solvent (DMSO)	0.49	0.56

After degassing the suspensions by stirring under vacuum, they were pressurized through the triple-layer orifice stainless steel spinneret (dimensions see Figure 1) with de-ionised water as the internal coagulant, extruding hollow fibre precursors into the external coagulant bath (tap water) separated by a ca. 0.23 m air gap, which prevented finger formation on the outer layer [23]. Upon contact with the internal and external coagulants, solvent exchange solidified the fibres, as the NiO, YSZ and polymer are insoluble in water. The extrusion rates of internal coagulant, inner layer and outer layer were 10.0, 7.0, 0.7-3.0 ml min^{-1}, respectively, controlled by syringe pumps.

Following straightening and drying of the NiO-YSZ|YSZ fibres, they were co-sintered in a box furnace (Elite Thermal Systems Ltd., UK) with the following sintering profile: binder burn out at 600 °C for 2 hours with a temperature ramp rate of 2 °C min^{-1}, followed by high temperature sintering at 1500 °C for 10 hours at 15 °C min^{-1} ramp rate and cooling to room temperature at 2 °C min^{-1}.

The outer electrode (length: 15 mm) was applied using brush coating (size 4/0, ProArte, England). The first layer was the functional electrode layer LSM-YSZ applied using a composite paste (NexTech Materials Ltd., USA) of 50/50 wt% $La_{0.8}Sr_{0.2}MnO_{3-\delta}$ (LSM) and YSZ, following drying on a hot plate at 60 °C for ca. 1 hour. A pure LSM layer (NexTech Materials Ltd., USA) was applied subsequently to enhance electrical conductivity and so minimise ohmic potential losses. After a further drying step, the fibres were sintered finally at 1100 °C for 3 hours with a temperature ramp of 4 °C min^{-1}.

Fibre characterization

Dilatometer studies. In preparation for the co-extrusion, the shrinkage behaviour of the dual layer components was investigated. NiO and YSZ were mixed at different weight percentages in ethanol, followed by drying at 80 ºC. These mixtures were then pressed into cylinders of ca. 5 mm diameter and 4 mm height using a hydraulic press with 1.25 t of applied pressure. Tests were performed in a dilatometer (NETZSCH, model DIL 402C) in static air heating the samples up to 1500 ºC with a temperature ramp rate of 5 ºC min^{-1}, dwelling the samples for 10 hours, followed by cooling down to room temperature.

Gas permeability. The gas-tightness was assessed using a nitrogen penetration method [24], whereby the pressure change over time for a sealed length of fibre was recorded. The permeability was calculated according to[i].

$$P = \frac{V}{RT \times A_m t} \ln\left(\frac{p_i - p_a}{p_f - p_a}\right) \quad (5)$$

Mechanical strength testing. The mechanical strength was assessed using a three-point bending method [25] utilising a tensile tester (Instron Model 4466) with a load cell of 5 kN and a sample holder distance of 30 mm. The bending strength was calculated according:

$$\sigma_f = \frac{8F_f L_f D_o}{\pi\left(D_o^4 - D_i^4\right)} \quad (6)$$

Porosity. The apparent porosity of the as-prepared precursors (NiO-YSZ|YSZ) and pre-reduced (Ni-YSZ|YSZ) fibres were calculated (Equation 7) from the absolute and envelope density measured using AccuPyc 1330 and Geopyc 1360 pycnometers (Micrometrics Instruments):

$$\varepsilon = 1 - \left(\frac{\rho_{envelope}}{\rho_{absolute}}\right) \quad (7)$$

Pore size analysis. The pore size distribution of the as-prepared precursors (NiO-YSZ|YSZ) and pre-reduced (Ni-YSZ|YSZ) fibres were determined using mercury porosimetry (Micrometrics, AutoPore IV, 9500).

Scanning electron microscopy and EDS. The microstructure of the micro-tubular solid oxide reactors were imaged using scanning electron microscopy. The exact dimensions of each fibre post-testing were confirmed using table-top scanning electron microscopes (TM-1000 and TM3030, Hitachi) at 15 kV accelerating voltage. Energy dispersive spectroscopy (EDS) was performed at 20 kV using a different SEM instrument (JSM 6400, JEOL, USA).

Reduction. The properties of un-reduced and reduced fibres were characterized and compared. Sintered NiO-YSZ|YSZ precursor fibres were reduced prior to analysis. The fibres were placed into a quartz tube and heated to 650 °C at 4 °C min-1 in a helium atmosphere (ca. 24 ml min^{-1}) in a tubular furnace (Elite Thermal Systems Ltd., UK). The precursors were then reduced for 2 hours in a H_2/He gas mixture (ca. 6/20 ml min^{-1}) and subsequently cooled down to room temperature in the same gas mixture to prevent any re-oxidation at 4 °C min^{-1}.

Electrochemical testing

Current collection, sealing and reactor assembly. Inner current collection was achieved by twisting the end of a 0.25 mm diameter silver wire (99.9% purity, annealed, VWR International LLC, UK) together and wrapping silver wool (99.9% purity, VWR International LLC, UK) around them before feeding this assembly through the lumen of the hollow

RSC Advances Accepted Manuscript

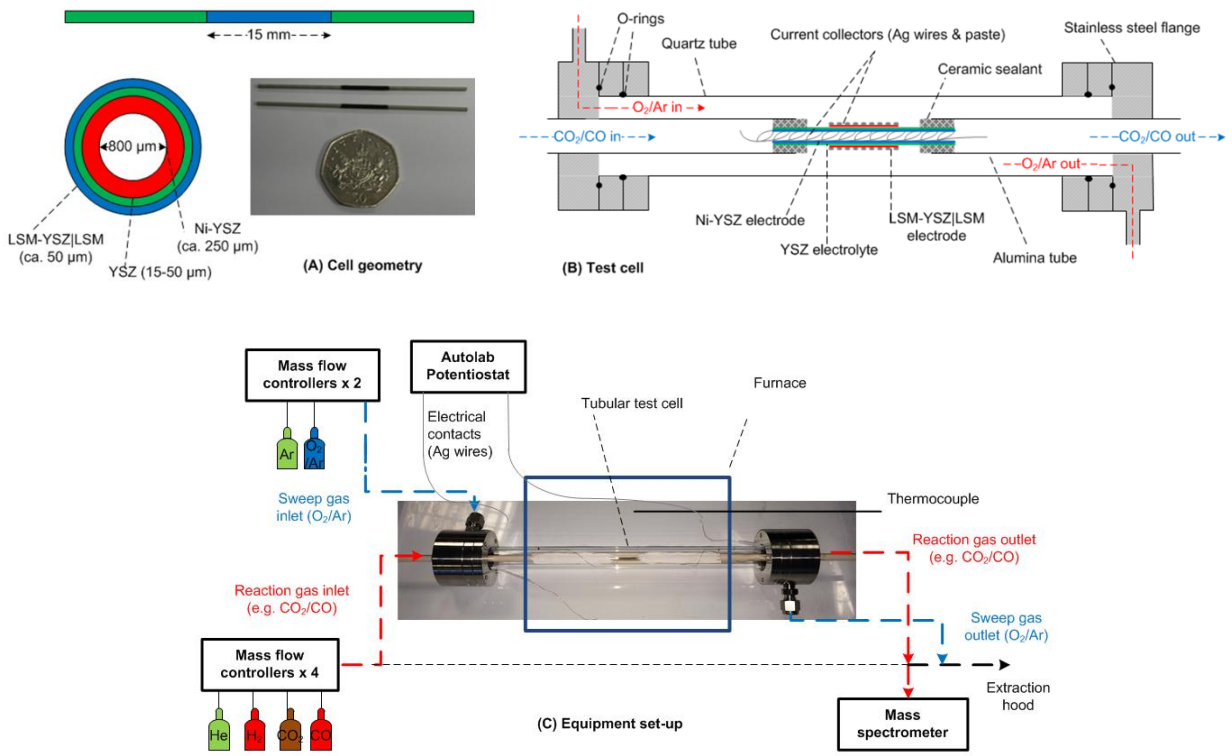

Figure 2: Complete reactor assembly: (A) cell geometry, (B) tubular test cell and (C) schematic of the experimental equipment.

fibre. Contact between wires/wool and the inner surface was enhanced by applying silver paste (VWR International LLC, UK). Silver wires of 0.2 mm diameter (99.99%, annealed, Advent Research Materials, UK) were wrapped around the outer electrode and fixed with silver paste. The length of individual silver wires from fibre to electrical connections was ca. 300 mm. Then the fibre was inserted into an alumina gas feed tube assembly and fixed with a ceramic cement (Ceramabond 552-VFG, Aremco, USA), which became gas-tight following successive heat treatments at 94 and 260 ºC for 2 hours with a heating rate of 4 ºC min-1. This reactor assembly was sealed into a 300 mm long quartz tube (20 mm OD, Multilab Ceramics, UK) with stainless steel end-caps made in-house, and sealed to the quartz tubes by Viton O-rings (Polymax, UK), as shown in Figure 2.

Electrolyser/Fuel cell Performance Tests. Reactor performance testing was performed directly after curing of the ceramic sealant in-situ. The reactor was heated in a tubular furnace (Elite Thermal Systems Ltd., UK) to 650 ºC at 4 ºC min^{-1}, while helium (ca. 24 ml min^{-1}) and 10% O_2 in argon (ca. 30 ml min^{-1}) were fed to the inner (Ni-YSZ) and outer electrode (LSM-YSZ|LSM), respectively. The nickel oxide was reduced to nickel at 650 ºC by exposure to a reducing gas atmosphere at the inner electrode (H_2/He gas mixture at 6/20 ml min^{-1}) for 2 hours. After reduction, the temperature was increased to the operating temperatures (700, 750 and 800 ºC), monitored by an N-type thermocouple. The operational gas feed compositions were 90/10 or 70/30 CO_2/CO[ii] with 40 ml min^{-1} total flow at the inner electrode and 10% O_2 in argon at 46 ml min^{-1} at the outer electrode; flow rates were controlled by automated mass-flow controllers (Bronkhorst, UK).

The silver wires were connected to a potentiostat/galvanostat equipped with a frequency response analyser (FRA) 4.9 module for electrochemical impedance measurements (PGSTAT302N, Metrohm Autolab B.V., Netherlands) and operated by electrochemical test procedures created in the Nova 1.10.2 software (Metrohm Autolab B.V., Netherlands).

The electrochemical experiments included measuring the potential difference response of the cell to linearly scanned applied current and steady state measurements over varying time scales at constant potential difference or constant current. The intrinsic electrical properties of materials and interfaces were characterized using electrochemical impedance spectroscopic (EIS) measurements at open circuit potential difference (OCPD) and operating potential differences (SOE or SOFC operating mode) in the frequency range of 10^5 – 0.1 Hz (with an RMS amplitude of 0.01 V or 0.001 A for potentiostatic or galvanostatic operation, respectively.)

On-line off-gas analysis of the fuel-side electrode gases was performed using mass spectrometry (Genesys 200D, ESS Ltd, UK) monitoring the reactant consumption / product formation, as well as detecting radial leakage across fibre imperfections.

RSC Advances Accepted Manuscript

 This journal is © The Royal Society of Chemistry 2012

Results and Discussion

Characterization of hollow fibre reactors

Sintering behaviour. Figure 3 shows the shrinkage behaviour of sintering pure YSZ and NiO and their cermet composition within the fuel electrode. This highlights a mismatch in the shrinkage of the cathode and electrolyte layer. The inner NiO-YSZ cermet layer shrank more and at a higher shrinkage rate with a lower temperature on-set, so exerting tensile stresses on the electrolyte and causing failure. This was detected in earlier batches of fibres, which broke during sintering, independently of sintering temperature, time, heating or cooling rates. However, due to percolation restrictions (ca. 40 vol% Ni corresponding to ca. 55 wt% NiO for solid state fabrication techniques [26]), the NiO content could not be decreased. Thus, to decrease the effect of the mismatch, the electrolyte thickness range was decreased from ca. 80-100 µm to 15-50 µm by adjusting the extrusion rates during the spinning process.

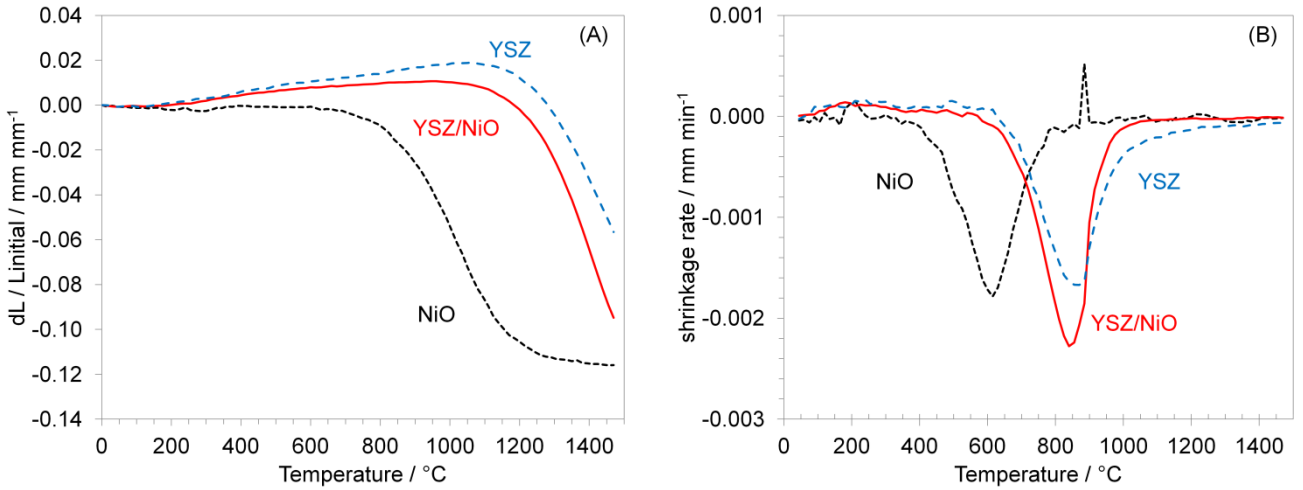

Figure 3: Sintering behaviour of NiO, 60/40wt% NiO-YSZ (fuel electrode layer) and YSZ (electrolyte) with (A) shrinkage and (B) shrinkage rate.

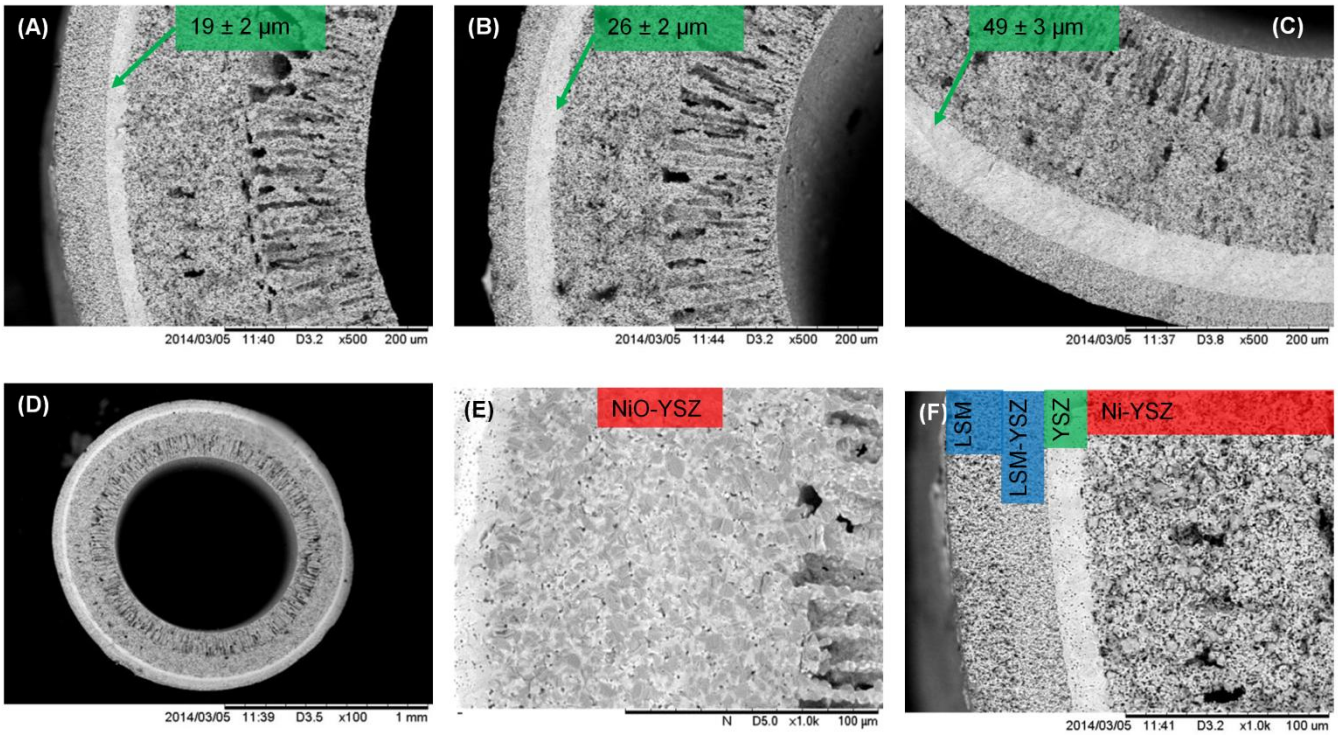

Figure 4: SEM images of cross-sectioned fibres post-operation – except (D): (A)-(C) reduced fibres with different electrolyte thicknesses, (D) reduced fibre – full cell, (E) un-reduced precursor fibre and (F) reduced fibre with (D)-(E) at 19 ± 2 µm electrolyte thickness.

RSC Advances Accepted Manuscript

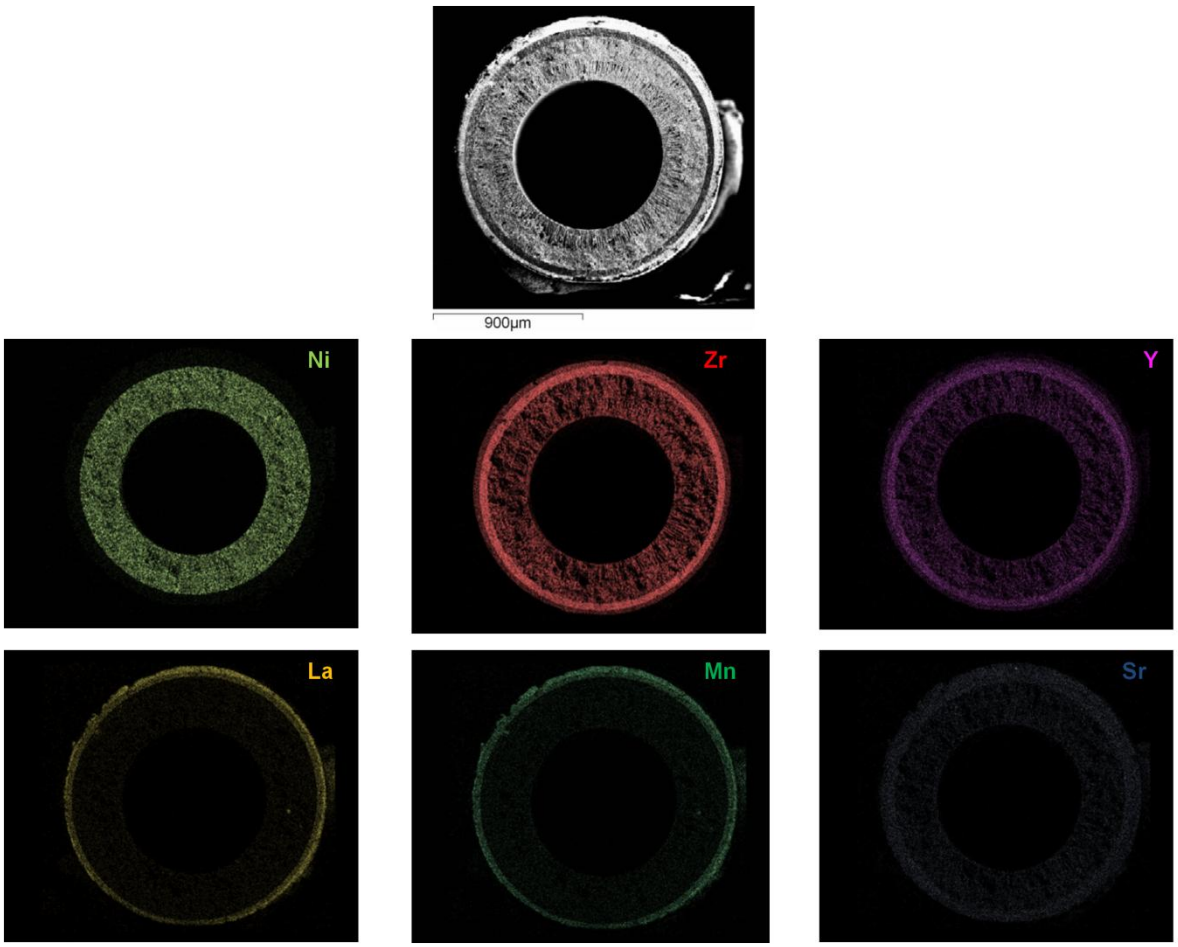

Figure 5: SEM image and EDS maps of individual elements within the Ni-YSZ|YSZ|LSM-YSZ|LSM micro-tubular solid oxide electrolyser (post-operation). Note: for a coloured version of these graphs the reader is referred to the online version of this paper.

MICROSTRUCTURE AND POROSITY. Figure 4A-F show the microstructures for different extrusion rates and resulting thicknesses. By varying the outer layer extrusion rates, the electrolyte thickness could be manipulated to be on average 19 (± 2), 26 (± 2) and 49 (± 3) µm, while the inner layer varied between ca. 250 to 210 µm for 19 to 49 µm electrolyte thicknesses. The inner electrode was asymmetrical with finger-like voids extending 49, 44 and 39% into the cathode layer (for 19, 26 and 49 µm electrolyte thickness, respectively), which was beneficial in enhancing mass transport rates into the electrode structure [27]. Comparing E (unreduced) and F (reduced) fibres, an increase in porosity within the bulk inner Ni-YSZ cermet electrode was visible. This sponge-type structure was a result of the reduction of nickel oxide to nickel and the consequent volume losses. Some pores were still visible within the electrolyte, but most were closed pores judging by results of gas permeability measurements, as discussed below, and so did not impact on the performance of the solid oxide reactors, except in decreasing effective conductivities.

The distributions of YSZ and NiO within the three layers were determined using energy dispersive X-ray spectroscopy (EDS). Figure 5 shows the maps of nickel, zirconium, yttrium, lanthanum, strontium and manganite across the hollow fibre cross-section (post-operation), showing homogeneous elemental distributions within the respective layers.

Figure 6 reports the effects of electrolyte thickness and NiO reduction on porosities of Ni(O)-YSZ|YSZ hollow fibres. For all electrolyte thicknesses, the reduced fibres were more porous than their unreduced precursor, as nickel (6.59 cm^3 mol^{-1}) has a lower molar volume than nickel oxide (11.20 cm^3 mol^{-1}). Porosity within the unreduced samples was due to the finger-like voids formed during the phase-inversion process. The apparent porosity decreased with electrolyte thickness for both reduced and un-reduced fibre. Firstly, this was due to the porosity reported including the electrolyte contribution (which was close to being 100 % dense) and the relative envelope volume of the electrolyte increased from ca. 8 to 23 % with increasing electrolyte thickness. Secondly, the finger-like voids

RSC Advances Accepted Manuscript

 This journal is © The Royal Society of Chemistry 2012

extended differently into the electrode layer depending on the electrolyte thickness: 49, 44 and 39 % for 19, 26 and 49 µm.

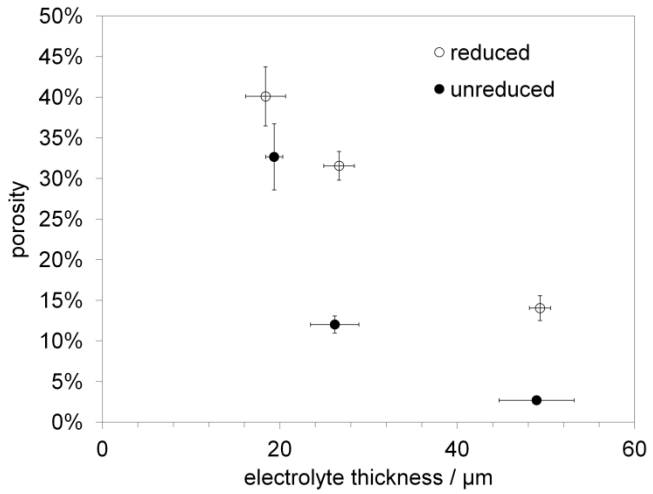

Figure 6: Porosity of unreduced and reduced hollow fibres as a function of electrolyte thickness.

Figure 7 shows the pore size distribution within the hollow fibres in their unreduced and reduced state for the 19 µm thick electrolytes. The pores with intrusion maxima at ca. 750 µm were associated with the large finger-like voids and were found within the reduced and unreduced samples. Contrastingly, smaller pores (maxima at ca. 60 and 200 nm) were formed as a result of the reduction of the nickel oxide to elemental nickel, creating the characteristic sponge-type structure within the bulk of the electrode. Similar trends were obtained for the 26 and 45 µm electrolyte thicknesses, albeit intrusion peaks were less well defined.

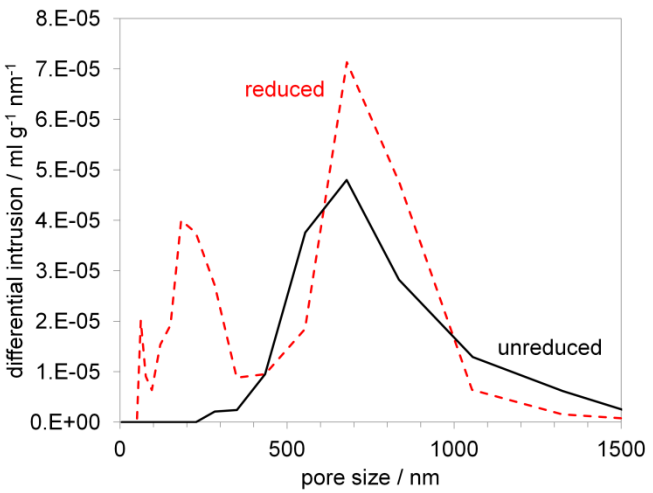

Figure 7: Pore size distributions within the hollow fibres before and after reduction (for 19 µm electrolyte thickness).

Mechanical and gas-tightness properties. The mechanical strength of individual fibres is crucial in determining long-term stability. Bending strengths of 161 (± 19) and 156 (± 26) MPa for the 19 and 26 µm (averaged sizes) electrolytes have been measured, which is comparable to Ni-YSZ|YSZ fibres reported within the literature [22]. However, the average bending strength for the 49 µm electrolytes was only 111 (± 44) MPa. Thicker electrolytes are expected to provide higher mechanical strength. However, as explained for the sintering behaviour, the shrinkage mismatch of NiO-YSZ and pure YSZ causes tensile stresses on the fibre resulting in breakage of fibres with thick electrolyte layers. Therefore the 49 µm electrolyte fibres are more likely to be affected by in homogeneities of the fibre dimensions shown by lower strength and wide spread within the measured data.

Ceramic gas-membranes are generally considered gas-tight at a nitrogen permeability of less than 10^{-10} mol m^{-2} s^{-1} Pa^{-1} [24]. This gas-tightness is crucial as solid oxide cells rely on spatially separated redox reactions, so gas cross-over is to be avoided. During MT-SOFC operation, gas leakage is usually detected by a decrease in the open circuit potential as the local gas composition at the electrodes changes: potential recombination of products decreasing the yield and in fuel cell mode reactants are consumed without power being generated. Figure 8 implies that as the thickness of the electrolyte was increased, so did the gas-tightness and the values approached the benchmark proposed by Tan *et al.* [24]. This was mainly due to the decreasing probability of pinholes protruding across the entire electrolyte thickness as that property was increased.

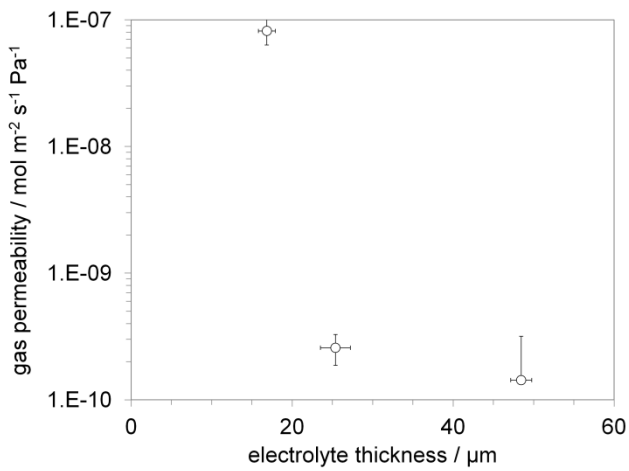

Figure 8: Gas tightness as a function of the electrolyte thickness.

Electrochemical performance

Performance of the MT-SOEs. The open circuit potential differences were predicted to be 0.886, 0.856 and 0.826 V for 700, 750 and 800 °C, respectively, using the Nernst equation (8). Deviations were measured between 56 (56) and 70 (75) mV for 50 to 15 µm electrolyte thickness, respectively, at 700°C (800°C) operating temperature. The 14 to 19 mV variation between different electrolyte thicknesses can be explained by the thinner electrolyte not being as gas-tight (Figure 9); higher temperatures resulted in increased deviations. The remaining

RSC Advances Accepted Manuscript

deviation was possibly due to air leakage through the ceramic sealant, as well as local variations in gas composition at the electrodes due to an unquantified aerodynamic flow field distribution.

$$\Delta E = \Delta E^{\ominus}_{CO_2/CO,T} + \frac{RT}{2F}\ln\left[\frac{p_{CO_2}}{p_{CO}\sqrt{p_{O_2}}}\right] \quad (8)$$

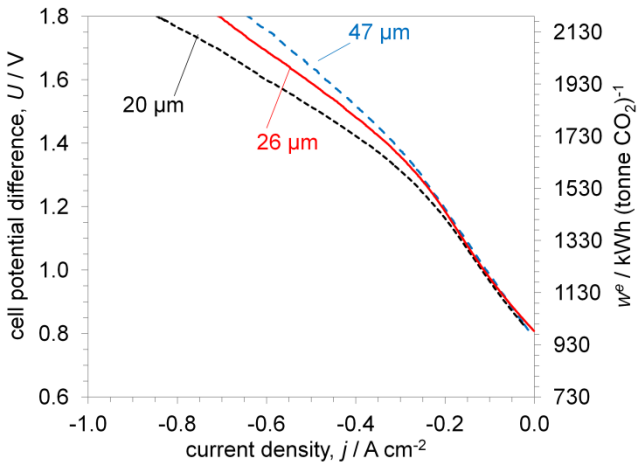

Figure 9: Effects of applied current density (j) and electrolyte thickness on cell potential difference (U) and specific electrical energy consumption (w^e) at 750 ºC and 90/10 CO_2/CO gas feed composition.

Figure 9 shows the effect of the current density[iii] on cell potential difference at 750 ºC for typical electrolysis cells with electrolyte thicknesses between 15 to 50 µm. The performance of the electrolyser increased as the electrolyte thickness was decreased, due to the decreased ohmic potential losses (Equation 9).

$$\Delta\phi^{IR}_{electrolyte} = \int_{r_e}^{r_e+t_e} \frac{j(r)}{\sigma_{e,T}}dr = \frac{I}{2\pi L_{electrode}\sigma_{e,T}}\ln\left(1+\frac{t_e}{r_e}\right) \quad (9)$$

The specific electrical energy consumption (Equation 10) highlights that operation at higher current densities would be beneficial, as the energy penalty for an incremental increase in current density is smaller than at lower current densities.

$$w^e_{CO_2} = \frac{2F}{\Phi^e_{CO_2}}\cdot\frac{U}{3.6M_{CO_2}} \quad (10)$$

Figure 10 reports the effects of current density and operating temperature (700, 750 and 800 ºC) on the cell potential difference and specific electrical energy consumption. Higher temperatures enhanced the performance of the electrolyser due firstly to increased ohmic conductivity of the electrolyte – 1.9, 2.9 and 4.3 S m^{-1} for 700, 750 and 800 °C, respectively [28] – and secondly to faster kinetics. Despite the controversy about the identity of the rate limiting steps within solid oxide electrolysers (or fuel cells) for CO_2, H_2O, H_2 or CO reduction/oxidation (single charge transfer step assumption using Butler-Volmer or elementary modelling approaches [29-31]); all reaction rates of the processes involved e.g. charge transfer, surface adsorption etc. usually follow an Arrhenius type relationship; hence higher temperatures are expected to decrease the overpotential required to achieve a pre-set current density.

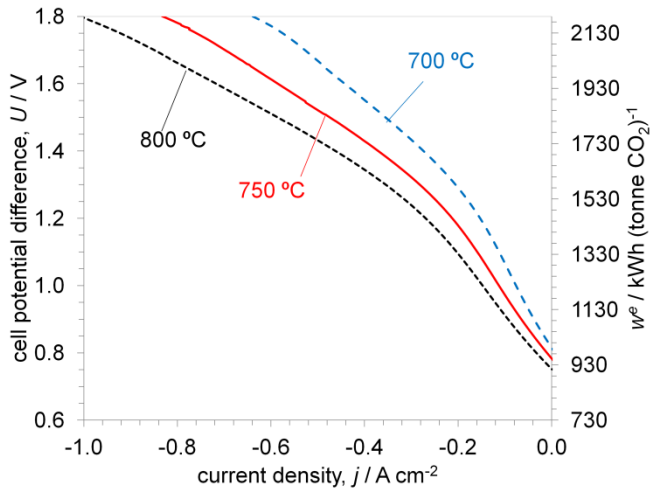

Figure 10 : Effects of applied current density (j) and operating temperatures on cell potential difference (U) and specific electrical energy consumption (w^e) for a 15 µm thick electrolyte and 90/10 CO_2/CO gas feed composition.

However, to further assess the effects of electrolyte thickness and operating temperature on electrolyser performance, electrochemical impedance spectra for the thickness and temperature extremes were measured, the results being reported in Figure 11. The high frequency intercepts represent the (area specific) ohmic resistance and the difference between high and low frequency intercepts is associated with a cell's overall (area specific) polarization resistance. The individual values are summarized in Table 2.

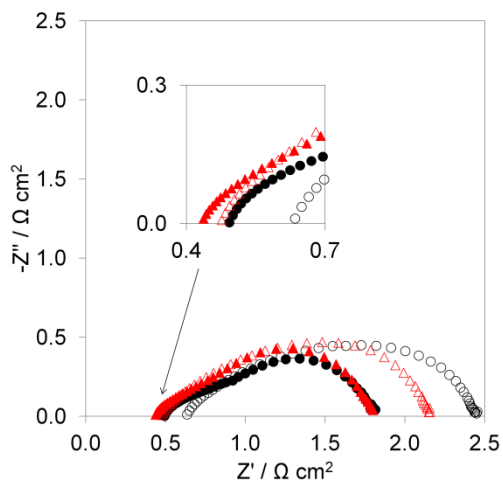

Figure 11. Electrical impedance spectra at 700 °C (unfilled) and 800 ºC (filled) for electrolyte thickness extremes: 15 (▲) and 50 (●) µm measured at OCPD.

RSC Advances Accepted Manuscript

This journal is © The Royal Society of Chemistry 2012

Table 2: Contributions to area specific resistances of tubular solid oxide cell.

	Ohmic resistance / Ω cm^2	Polarisation resistance / Ω cm^2	Total resistance / Ω cm^2
15 µm – 700 ºC	0.47	1.69	2.16
15 µm – 800 ºC	0.43	1.37	1.80
50 µm – 700 ºC	0.63	1.82	2.45
50 µm – 800 ºC	0.49	1.32	1.81

The (area specific) ohmic resistances decreased with decreasing electrolyte thickness, as expected from equation 8. Likewise, increasing temperatures decreased (area specific) ohmic potential losses due to higher conductivities of the YSZ electrolyte. However, calculating the individual contributions to the total ohmic potential losses [32] (Equations 10-12 and Table 3) due to: wire resistance, contact losses, anode and cathode losses, only 28-5% of the total resistance were due to the electrolyte resistance (Figure 12).

$$\Delta\phi_{total}^{IR} = \int_{r_e}^{r_e+t_e} \frac{j(r)}{\sigma_e} dr + \frac{I_{cell} L_{wire}}{A_{wire}\sigma_{wire}} + \Delta\phi_{contact}^{IR} + \int_{r_{inner}}^{r_e} \frac{j(r)}{\sigma_{Ni\,electrode}} dr + \int_{r_e+t_e}^{r_{outer}} \frac{j(r)}{\sigma_{LSM\,electrode}} dr \quad (10)$$

$$\sigma_e = \frac{\sigma_{0,electrolyte}}{T} \exp\left(\frac{-E_{electrolyte}}{RT}\right) \quad (11)$$

$$\Delta\phi_{contact}^{IR} = I_{cell} R_o - \Delta\phi_{electrolyte}^{IR} - \Delta\phi_{wires}^{IR} \quad (12)$$

Table 3: Parameters used to calculate ohmic potential loss contributions (set or obtained from literature).

Parameter	*Value*	*Comments*	*Reference*
A_{wire} / m	4.9 x 10^{-8}	(0.25 mm OD – used for inner electrode)	
	3.1 x 10^{-8}	(0.20 mm OD – used for inner electrode)	
L_{wire} / m	0.1	within furnace	
	0.2	outside furnace	
r_{inner}, r_e, t_e, r_{outer} / m	4.1, 6.6, 0.15, 7.5 (x 10^{-4})	Fibre 1 (15 µm)	
	4.3, 6.3, 0.5, 7.2 (x 10^{-4})	Fibre 2 (50 µm)	
σ_{wire} / S m^{-1}	6.14 x 10^7	outside furnace (298 K)	[33]
	3.32 x 10^7	averaged over temperature gradient within furnace	[33]
$\sigma_{Ni\,electrode}$ / S m^{-1}	8.0 x 10^3	(973 K)	[34]
	9.2 x 10^3	(1073 K)	
$\sigma_{LSM\,electrode}$ / S m^{-1}	6.6 x 10^3	(973 K)	[34]
	7.0 x 10^3	(1073 K)	
$\sigma_{o,electrolyte}$ / S m^{-1}	3.6 x 10^7		[28]
$E_{electrolyte}$ / J mol^{-1}	8.0 x 10^4		[28]

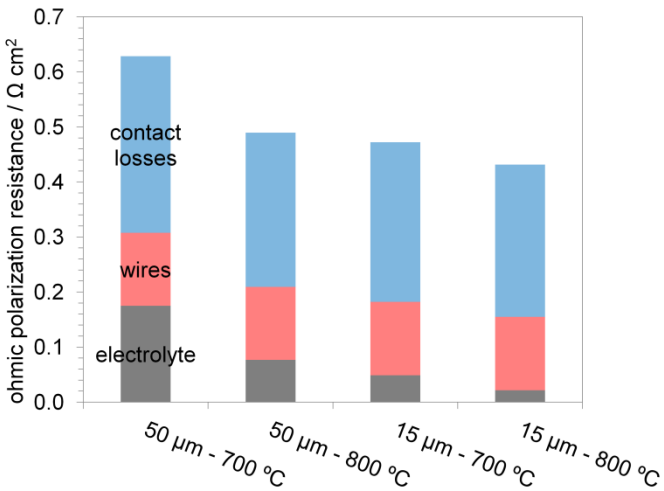

Figure 12 : Individual contributions to the area specific ohmic resistance as a function of operating temperature and electrolyte thickness. Note: the combined ohmic resistance due to the cathode and anode are less than 0.07% of the total resistance, so are omitted from this figure.

Thinning the electrolyte from 50 to 15 µm decreased the resistance contribution by 11-18%, depending on the operating temperature. The resistance of the wires and contact potential losses were dominant, especially at elevated temperatures. Careful reactor design has to be implemented for scale-up and stack design to decrease resistance due to wires, *i.e.* shorter and thicker wires where possible. The current collection is a more challenging problem, solutions to which are the subject of on-going investigations. For example, promising developments are the co-extrusion of an additional current collection layer [35].

The area specific electrode polarization resistances at OCPD for the different thicknesses were expectedly similar, as they were associated with charge and mass transfer reactions, which should be independent of electrolyte thickness. They decreased with increasing temperature due to enhanced kinetics, as discussed earlier.

A strong dependence of the total area specific resistance (ASR) as a function of the current density / cell potential difference was derived by analysing the change in slopes in Figure 9 or Figure 10 and highlighted in Figure 13. A peak in ASR was detected at ca. 1.0-1.2 V cell potential difference, depending on temperature and gas-composition. This change in overall resistance was believed to be due to the overall electrolysis reaction being endothermic, whereas Joule heating increases the cell temperature, resulting in a minimum temperature between the OCPD and the thermo-neutral potential difference (TNPD – ca. 1.46 V, as discussed in section 3.2.2, equation (16)); similar observations have been discussed by Yan *et al.* [36].

RSC Advances Accepted Manuscript

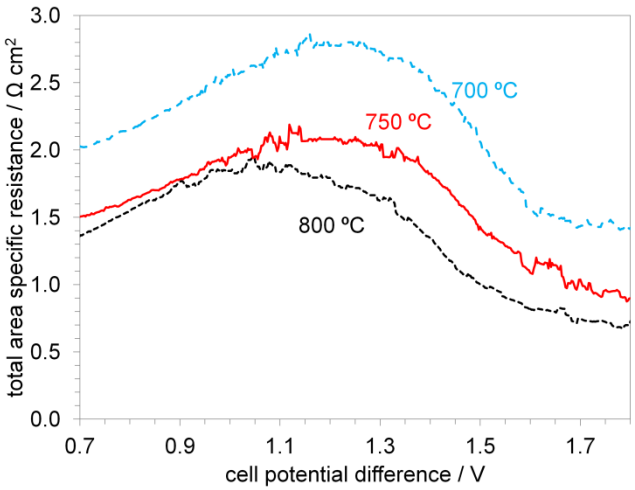

Figure 13: Effects of cell potential difference and temperature on area specific resistance for a 50 µm thick electrolyte and 90/10 CO_2/CO gas feed composition.

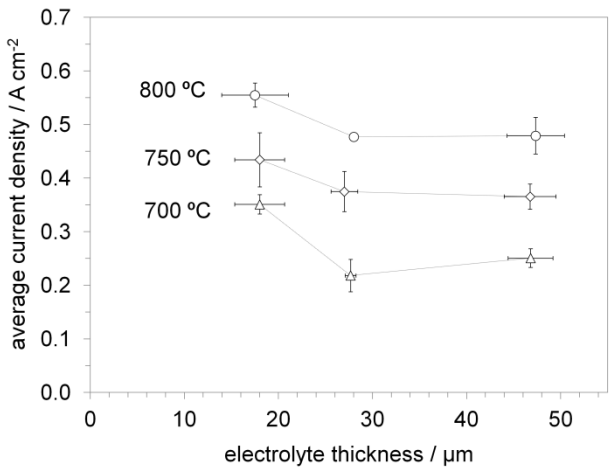

Figure 14. Effects of electrolyte thickness and temperature on average current densities for a cell potential difference of 1.5 V; data averaged over 1-5 cells.

Current densities of ca. 1 A cm^{-2} were achieved at 1.8 V, for 800 °C and with a 15 µm thick electrolyte. In comparison, the best performing planar cells achieve this current density between 1.2 V (0.8 A cm^{-2} – 850 °C) to 1.25 V (1.0 A cm^{-2} – 800 °C) [5,7], which corresponds to 27-31% less electrical energy consumption. However, as discussed above, the main limitations of the MT-SOEs at present are the current collection and contact losses, which contribute 72-95% towards the ohmic potential losses. Furthermore, Zhan and Zhao [7] operated their electrolyser in co-electrolysis mode, using a CO_2/H_2 gas feed due to the reverse water gas shift reaction (Equation 13), which has been reported to achieve higher performance[37].

$$CO_2 + H_2 \underset{\text{water gas shift reaction}}{\overset{\text{reverse water gas shift reaction}}{\rightleftharpoons}} H_2O + CO \qquad (13)$$

However, the performance of the MT-SOEs reported here exceeds what has been reported for other tubular systems: 0.38 A cm^{-2} (CO_2 electrolysis – this study) compared to 0.20 A cm^{-2} (co-electrolysis) [19] at 1.4 V and 750 °C. Dipu *et al.* [38] recently also reported results for electrolysis of CO_2 alone; however, their maximum current densities at 2.0 V were very low: 1.5 – 3.5 mA cm^{-2} for 800-900 °C, respectively, which can be attributed to their 1.5 mm thick YSZ electrolyte.

Figure 14 depicts the current densities at a cell potential difference of 1.5 V averaged over multiple fibres at different operating temperatures and electrolyte thicknesses. In general, similar trends as depicted in Figure 10 and Figure 11 could be verified across the batch of hollow fibres.

The reactant consumption and product formation can be determined from analysis of the electrolyser off-gas for steady state measurements at individual potentials. The theoretical product rates can be predicted using Faraday's law, assuming CO_2–CO conversion is the only reaction (Equation 14):

$$I = 2F\frac{dn}{dt} \qquad (14)$$

The measured and predicted values are shown in Figure 15. Up to 1.7 V, the maximum cell potential differences investigated, the change in CO_2 and CO correspond to the predicted values (within experimental errors due to the 'noise' of ion currents in the mass spectrometer), indicating 100% charge yields. Analysing the microstructure images, no carbon formation could be detected[iv]. Furthermore, coking via the Boudouard reaction (Equation 15) is unlikely, as the equilibrium composition of CO_2/CO before and during electrolysis were below the equilibrium CO fraction of 0.57 to 0.86 for 700 to 800°C, respectively, and cold-zones were avoided by operating at the thermoneutral potential difference in short-term degradation studies.

$$2CO \rightleftharpoons C + CO_2 \qquad (15)$$

The cell potential differences were deliberately chosen to be below 1.8 V to avoid the parasitic losses reported at higher potentials due to electronic short-circuiting through the YSZ electrolyte. In the range of operating temperatures, the electronic conductivity of the electrolyte is 2.1-9.2 % and 22.5-79.9 % the value of the ionic conductivity at 1.8 and 2.0 V, respectively [9]. Furthermore, operation at even higher potentials > 2.5 V would cause irreversible damage to the electrolyte due to reductive decomposition of the zirconium oxide [9, 39].

RSC Advances Accepted Manuscript

This journal is © The Royal Society of Chemistry 2012

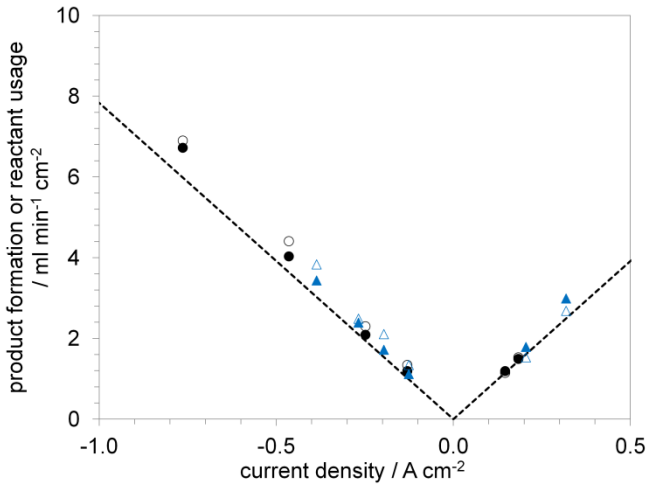

Figure 15: Effect of current density on CO_2-CO compositional change for 90/10 CO_2/CO gas feed for 50 µm thick electrolyte at 700 °C (▲) and 800 °C (●) with CO_2 (unfilled) and CO (filled), compared to theoretical conversion (- - -).

Short-term performance degradation testing. Short-term degradation studies of the MT-SOEs were performed at a constant current of 0.3 A cm^{-2}, the resulting cell potential difference (ca. 1.46 V) being close to the thermoneutral potential difference of 1.464 V (Equation 16). No visible degradation could be detected over 8 hours, indicating fracture-free manufacture.

$$E_{tn} = \frac{\Delta H_r}{2F} \tag{16}$$

Examining the results more closely, it can be noticed that the cell required about 2 hours to stabilize (fluctuations of up to 10 mV were measured during this phase), which was also evident from the disappearance of noise at low frequencies in the corresponding impedance spectra (data not shown here). After stabilization, the rate of degradation was ca. 2 mV hr^{-1}. The initial stabilization could be associated with fully activating the electrodes in reduction mode, as the cell was previously exposed to cyclic operation switching between reductive and oxidative conditions. Possible causes of degradation have been discussed in the literature, including blocking of the triple phase boundary with impurities in the gas stream (e.g. H_2S) [40]. Over 9 000 hours of operation, 3.8% (40 mV) (1000 hr)$^{-1}$ increase in operating potential difference was reported for steam electrolysis, which also takes into account degradation due to operational incidences [41]. However, to establish the cause and extent of degradation of the MT-SOE in this study, longer testing durations are required in future experiments, together with thermal and redox cycling, as reported for MT-SOFCs [42, 43].

Performance in dual-mode operation (SOE and SOFC). The reversibility of these cells was also investigated by cycling between electrolyser and fuel cell modes (Figure 16). Assuming essentially unity charge yields of reaction 1 in both SOE and SOFC modes, round-trip efficiencies of maximum 72% and 32% for 0.1 and 0.3 A cm^{-2} at 800 °C where calculated according:

$$\Phi^{e}_{CO-O_2} = \frac{U_{fuel\ cell}}{U_{electrolyser}} \tag{17}$$

Notably, the gas feed composition had a greater effect in fuel cell mode. However, higher CO concentrations can promote coke formation, so are undesirable [44]. Thus, for experiments involving such cycling, rich and lean gases should be employed for electrolyser and fuel cell modes, respectively, as has been proposed in a recent modelling study [45]. Peak power densities of about 0.12 (0.08) to 0.13 (0.10) W cm^{-2} for 90/10 and 70/30, respectively, at 800 °C (700 °C) were comparable to values reported in the literature for YSZ electrolyte based cells operating mainly with H_2 (some operating on natural gas) [32,46,47], especially as the gas mixtures were optimized for electrolyser operation.

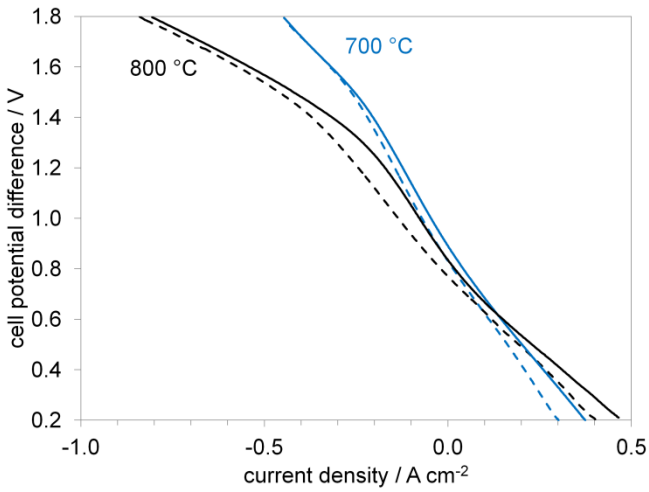

Figure 16: Effects of applied current density and operating temperature on cell potential difference using a 50 µm thick electrolyte for 90/10 (---) and 70/30 (—) CO_2/CO gas feed composition at 700 and 800 °C.

In view of possible applications to load levelling, short-term switching stability between fuel cell and electrolyser mode was also investigated (Figure 17). For each cycle, EIS data were collected at the start and end of the measurements at the operating current density of 0.1 A cm^{-2}. The cell potential difference during electrolysis mode initially stabilized quickly. However, following cycles of fuel cell operation, the stabilization took longer, albeit similar potential differences (1.32, 1.42 and 1.32 V for cycle 1-3, respectively) were eventually reached. Contrastingly, the cell potential difference in fuel cell mode degraded by ca. 20 mV over 1 hour, worsening in subsequent cycles (> 70 mV), which was also reflected in the large increase of area specific electrode polarization resistance shown in the impedance spectra (shift of the high frequency intercept), whereas the ohmic polarisation resistance stayed constant. Possible explanations are: (a) mass transport limitations, (b) degradation of the cell. At 0.1 A cm^{-2}, reactant utilisation was 19.6% and 7.8 % for CO and O_2,

RSC Advances Accepted Manuscript

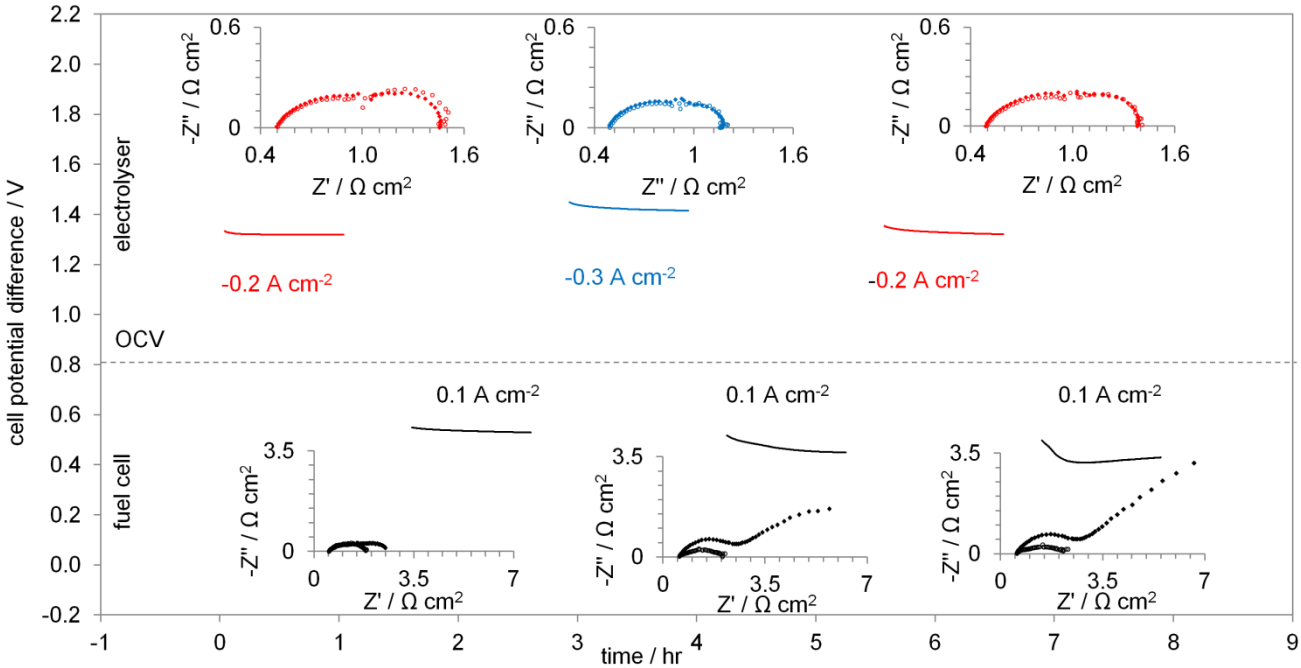

Figure 17: Effect of time on cell potential difference for MT-SOE at 750 ºC, 90/10 CO2/CO gas feed and 19 µm thick electrolyte, cycling between electrolysis and fuel cell operation at current densities in the range of ca. -0.3 to +0.1 A cm^{-2}. (Note: electrical impedance spectra were recorded at the applied current densities at the start (unfilled) and end (filled) of each cycle with a frequency range of 10^5 – 0.1 Hz with an RMS amplitude of 0.001 A).

respectively (not accounting for recombination losses due to leakage). The mass transport limited current density can be calculated using Equations 18-21, with the relevant parameters given in Table 4.

Table 4: Parameters used to calculate the mass transport limiting current (set or obtained from literature).

Parameter	*Value*	*Comments*	*Reference*
p_{total} / Pa	1.01 x 10^5		
$v_{e,\,anode}$	2	Equation 1	
$v_{e,\,cathode}$	4	Equation 2	
t_{anode} / m	2.5 – 2.1 x 10^{-4}		
$t_{cathode}$ / m	0.5 x 10^{-4}		
$D_{CO\text{-}CO2}$ / m^2 s^{-1}		Calculated following procedure outlined in reference [48]	[48]
$D_{O2\text{-}Ar}$ /m^2 s^{-1}			
ε_{anode}	0.4 – 0.15	Ni-YSZ electrode (range adopted from Figure 6)	
$\varepsilon_{cathode}$	0.2	LSM-YSZ electrode	[32]
τ_{anode}	3		[49]
$\tau_{cathode}$	3		[49]
$\dot{V}_{total}$, $\dot{V}_{initial,\,CO}$ / ml min^{-1}	40, 4 (Base case) 40, 12 (Variation 1)	90/10 CO_2/CO feed 70/30 CO_2/CO feed	
$\dot{V}_{total}$, $\dot{V}_{initial,\,O2}$ / ml min^{-1}	46, 4.6 (Base case) 75, 7.5 (Variation 1)	10/90 O_2/Ar feed 10/90 O_2/Ar feed	

$$j_{L,\,anode} = \frac{p_{total} x_{CO}^{bulk} D_{CO}^{eff} v_{e,\,anode} F}{RTt_{anode}} \quad (18)$$

$$j_{L,\,cathode} = \frac{p_{total} x_{O_2}^{bulk} D_{O_2}^{eff} v_{e,\,cathode} F}{RTt_{cathode}} \quad (19)$$

$$D_{CO}^{eff} = \frac{\varepsilon_{anode}}{\tau_{anode}} D_{CO-CO_2} \quad (20)$$

$$D_{O_2}^{eff} = \frac{\varepsilon_{cathode}}{\tau_{cathode}} D_{O_2-Ar} \quad (21)$$

However, the mole fraction changes as the reactions proceed, which can be calculated using Equation 22 in conjunction with Faraday's law (Equation 14).

$$x_i^{bulk,\,final} = \frac{\dot{V}_{initial}^{i} - \dot{V}_{final}^{i}}{\dot{V}^{total}} \quad (22)$$

Table 5: Mass transport limited current densities at 1073 K.

	$j_{L,\,anode}$ *(high porosity)* / A cm^{-2}	$j_{L,\,anode}$ *(low porosity)* / A cm^{-2}	$j_{L,\,cathode}$ / A cm^{-2}
Scenario 1	1.71	0.76	10.30
Scenario 2	0.73	0.47	2.33
Scenario 3	2.18	1.42	3.81

Scenario 1 is the base-case neglecting limitations due to conversion. Scenario 2 and 3 solve iteratively for the conversion depletion and transport limited current densities at different CO and O_2 flow rates (denoted Base case and Variation 1 in Table 4).

RSC Advances Accepted Manuscript

This journal is © The Royal Society of Chemistry 2012

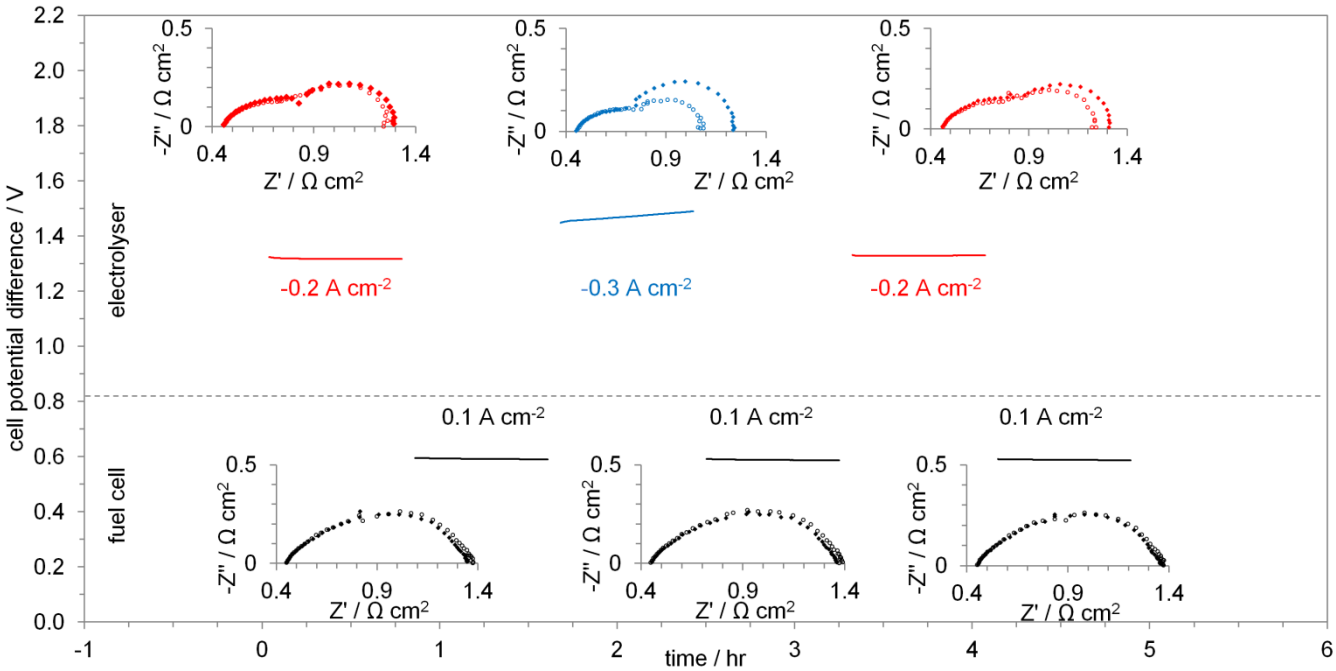

Figure 18: Effect of time on cell potential difference for MT-SOE at 750 °C, 70/30 CO_2/CO gas feed, total 10% O_2 in argon flow rate 75 ml min^{-1} and ca. 28 µm thick electrolyte, cycling between electrolysis and fuel cell operation at current densities in the range of ca. -0.3 to +0.1 A cm^{-2}. (Note: electrical impedance spectra were recorded at the applied current at the start (unfilled) and end (filled) of each cycle with a frequency range of 10^5 – 0.1 Hz with an RMS amplitude of 0.001 A.)

Table 5 shows that if reactant depletion due to conversion is taken into account, the applied current density of 0.1 A cm^{-2} is 14-21% of the mass transport limited current density with the fuel side being the limiting factor. Therefore, mass transport limitations could not have been the only factor leading to increased cell potential differences and area specific resistance degradation. However, the flow field at the oxygen electrode was not optimized, whereas the CO/CO_2 mix at the fuel electrode is forced to pass through the entire length of the reactor; bypassing of O_2/Ar within the quartz tube can occur, creating oxygen deficient regions close to the electrode.

Degradation of the electrodes could have been due either to oxygen being driven out of the LSM electrode in SOE mode, creating oxygen deficiency or an oxidised passivating layer on the nickel electrode in SOFC mode. As performance during SOE mode following SOFC mode was unaffected; *i.e.* the degradation was reversibly, decomposition of the LSM seems unlikely. The partial pressure of CO for Ni re-oxidation by CO_2 to occur needs to be lower than ca. 0.003 [50]. At 0.1 A cm^{-2}, the bulk partial pressure of CO was 0.092; however, a lower p_{CO} is expected at the electrodes, so partial re-oxidation of Ni seems possible. This hypothesis is supported by a longer time was required to reach steady state following fuel cell operation, *i.e.* possibly due to reversing the passivation process by reducing the Ni(NiO) cathode electrochemically again.

Performance in fuel cell mode stabilized when the O_2/Ar flow rate was increased by 63 % to 75 ml min^{-1} and the CO_2/CO ratio changed to 70/30; hardly any degradation was then evident, with 0.59 V resulting at 0.1 A cm^{-2} for all three cycles (Figure 18) and the total resistance measured using EIS remained constant. Referring to Table 5, operating at these conditions also predicts higher cathode mass transport limited current densities, 3 and 0.33-fold increase for anode and cathode, respectively. However, degradation was slightly accelerated at higher current densities in electrolysis mode (40 mV at -0.3 A cm^{-2}), but appeared reversible at lower current densities, since for cycles 1 and 5, similar cell potential differences (1.32 and 1.33 V, respectively) were recorded. However, this again highlights the requirement that, if cells are to be run in both operational modes for load-levelling purposes, appropriate gas compositions should be chosen. Using the same gas compositions for fuel cell and electrolysis mode will cause at least one mode to under- perform and increase degradation rates.

Conclusions

Micro-tubular solid oxide electrolysers with compositions Ni-YSZ|YSZ|LSM-YSZ were fabricated successfully using a two-step process employing dual-layer co-extrusion phase inversion to fabricate the electrode | electrolyte hollow fibres, which after co-sintering were coated with the outer electrode and sintered again. Three distinct electrolyte thicknesses were produced: 19 (±2), 26 (±2) and 49 (± 3) µm. As expected, the CO_2 electrolyser performance increased with increasing temperature (700-800 °C) and decreasing electrolyte thickness. A current density of 1 A cm^{-2} at 1.8 V was achieved at 800 °C for a

RSC Advances Accepted Manuscript

15 µm electrolyte. 100 % charge yield was measured during steady state runs up to 1.7 V. Short-term degradation was shown to be slow (2 mV hr^{-1}) and the feasibility was established of reversible cycling operation between electrolysis and fuel cell modes, whereby different gas feed compositions were required to optimize the performance for either operational mode. Future work includes (a) varying the gas feeds to study the feasibility of co-reduction of CO_2 and steam within MT-SOEs, (b) improve the current collection to decrease the contact potential losses, which presently account for 51-64% of the total ohmic potential losses and (c) investigate longer-term degradation rates.

Acknowledgements

The authors gratefully acknowledge the Engineering and Physical Science Research Council (EPSRC) for funding for L.K (Grant: EP/K035274/1) and T.L. (Grant: EP/G012679/1).

Notes and references

[a] Chemical Engineering Department, Imperial College London, South Kensington, London SW7 2AZ, United Kingdom.

[i] The original method by Tan *et al.* [24] was for a single layer fibre. As the inner layer of the dual layer is porous by design, the membrane area calculations were based only on the electrolyte layer.

[ii] CO was co-fed to the electrolyser to prevent re-oxidation of the nickel at open-circuit potential difference.

[iii] Note: for all current density calculations, the inner radius of the fibre has been used to determine the electrode area unless stated otherwise. The fibre dimensions have been determined from SEM images for each individual reactor to ensure accuracy of the measurements for reliable comparison between different fibres.

[iv] Preliminary degradation studies at the thermoneutral potential difference showed no noticeable variation with time in the electrochemical impedance spectra after an initial stabilization process. As EIS is a very sensitive technique, changes in the microstructure or contamination due to coking should have been detected if present, although experiments over 100s-1000s hours are required to validate this.

1 Parliamentary Office of Science and Technology, 2008, Electricity Storage. http://www.parliament.uk/documents/ post/postpn306.pdf [Accessed 03/04/2013].
2 National grid, 2012, Historical Demand Data: Demand_Jan 2010 to Dec 2012. http://www2.nationalgrid.com/uk/industry-information/Electricity-transmission-operational-data/Data-Explorer/ [Accessed 18/03/2014].
3 Goeppert, M. Czaun, G.K.S. Prakash, G.A. Olah, Energy Environ. Sci,, 2012, 5, 7833.
4 S.H. Jensen, P.H. Larsen, M. Mogensen, Int. J. Hydrogen Energy, 2007, 32, 3253.
5 S.D. Ebbesen, M. Mogensen, J. Power Sources, 2009, 193, 349.
6 F.Bidrawn, G. Kim, G. Corre, J.T.S. Irvine, J.M. Vohs, R.J. Gorte. Electrochem Solid St., 2008, 11, B167.
7 Z. Zhan, L. Zhao, J. Power Sources, 2010, 195, 7250
8 P. Kim-Lohsoontorn, J. Bae, J. Power Sources, 2011, 196, 7161.
9 C-Y. Cheng, G.H. Kelsall, L. Kleiminger, J. Appl. Electrochem., 2013, 43, 1131.
10 McEvoy, Edited S.C. Singhal, K. Kendall. High Tmperature Solid Oxide Fuel Cells: Fundamentals, Design and Applications. 2003, First Edition, Elsevier, UK, 154.
11 K. Kendall, Int. J. Appl. Ceram. Technol., 2010, 7, 1.
12 Y. Du, N.M. Sammes, J. Power Sources, 2004, 136, 66.
13 W. Dönitz, E. Erdle, Int. J. Hydrogen Energy, 1985, 10, 291.
14 K. H. Quandt, R. Streicher, Int. J. Hydrogen Energy, 1986, 11, 309.
15 N.J. Maskalick, Int. J. Hydrogen Energy, 1986, 11, 563.
16 L. Shao, S. Wang, J. Qian, X. Ye and T. Wen, Int. J. Hydrogen Energy, 2013, 38, 4272.
17 Z. Wang, M. Mori and T. Araki, Int. J. Hydrogen Energy, 2010, 35, 4451.
18 C. Yang, C. Jin, F. Chen, Electrochimica Acta, 2010, 56, 80.
19 C.J. Moyer, N.P. Sullivan, H. Zhu and R.J. Kee, J. Electrochem. Soc., 2011, 158, B117.
20 M.H.D. Othman, Z. Wu, N. Droushiotis, U. Doraswami, G.H. Kelsall, K. Li, J. Membr. Sci., 2010, 351, 196.
21 M.H.D. Othman, N. Droushiotis, Z. Wu, G. Kelsall, K. Li, Adv. Mater., 2011, 23, 2480.
22 X. Meng, X. Gong, Y. Yin, N.-T. Yang, X. Tan, Z.-F. M., Int. J. Hydrogen Energy, 2013, 38, 6780.
23 B.F.K. Kingsbury, K. Li, J. Membrane Science, 2009, 328, 134.
24 X. Tan, Y. Liu and K. Li, AIChE J., 2005, 51, 1991.
25 S. Liu, K. Li, R. Hughes, Ceram. Int., 2003, 29, 875.
26 S.K. Pratihar, A. Dassharma, H.S. Maiti, Materials Research Bulletin, 2005, 40, 1936.
27 M.H.D. Othman, N. Droushiotis, Z. Wu, G. Kelsall, K. Li, J. Power Sources, 2012, 205, 272.
28 H. Zhu, R.J. Kee, J. Power Sources, 2003, 117, 61.
29 M. Ni, J. Power Sources, 2012, 202, 209.
30 Y. Shi, Y. Luo, N. Cai, J. Qian, S. Wang, W. Li, H. Wang, Electrochimica Acta, 2013, 88, 644.
31 D.G. Goodwin, H. Zhu, A.M. Colclasure, R.J. Kee, J. Electrochem. Soc., 2009, 156, B1004.
32 N. Droushiotis, A. Hankin, C. Rozain, G.H. Kelsall, J. Electrochem. Soc., 2014, 161, F271.
33 R.A. Matula, J. Phys. Chem. Ref. Data, 1979, 8, 1147.
34 N. F. Bessette II, W. J. Wepfer, J. Winnick, J. Electrochem. Soc., 1995, 142, 3792.
35 T. Li, Z. Wu, K. Li, J. Power Sources, 2014, 251, 145.
36 J. Yan, H. Chen, E. Dogdibegovic, J.W. Stevenson, M. Cheng, X-D. Zhou, J. Power Sources, 2014, 252, 79.
37 P. Kim-Lohsoontorn, N. Laosiripojana, J. Bae, Curr. Appl. Phys., 2011, 11, S223.
38 L. Dipu, Y. Ujisawa, J. Ryu, Y. Kato, Nucl. Eng. Des., 2014, 271, 30.
39 W. Weppner, J. Electroanal. Chem., 1977, 84, 339.
40 S.D. Ebbesen, J. Høgh, K.A. Nielsen, J.U. Nielsen, M. Mogensen, Int. J. Hydrogen Energy, 2011, 36, 7363.
41 J. Schefold, A. Brisse, F. Tietz, J. Electrochem. Soc., 2012, 159, A137.
42 N. Droushiotis, U. Doraswami, D. Ivey, M.H.D. Othman, K. Li, G.H. Kelsall, Electrochem. Commun. 2010, 12, 792.
43 N. Droushiotis, Ph.D. Thesis, Imperial College, 2012.
44 C. Stoots, J. O'Brien, J. Hartvigsen, Int. J. Hydrogen Energy, 2009, 34, 4208.

RSC Advances Accepted Manuscript

 This journal is © The Royal Society of Chemistry 2012

45 P. Kazempoor and R.J. Braun, Int. J. Hydrogen Energy, 2014, 39, 5955.
46 V. Lawlor, J. Power Sources, 2013, 240, 421.
47 K.S. Howe, G.J. Thompson, K. Kendall, J. Power Sources, 2011, 196, 1677.
48 E.N. Fuller, P.D. Schettler, J. C. Giddings, Ind. Eng. Chem., 1966, 58, 18.
49 S. Campanari, P. Iora, J. Power Sources, 2004, 132, 113.
50 D.D. Wagman, W.H. Evans, V.B. Parker, R.H. Schumm, I. Halow, S.M. Bailey, K.L. Churney, R.L. Nuttall, 1982, J. Phys. Chem. Ref. Data, 11, Suppl. 2.

RSC Advances Accepted Manuscript